Asian Journal of Chemistry; Vol. 38, No. 11 (2026), 3040-3052
ASIAN JOURNAL OF CHEMISTRY
https://doi.org/10.14233/ajchem.2026.36790

Fabrication of Highly Efficient ZnO-*g*-C_3N_4-AgI Ternary Heterojunction for Antimicrobial and Photocatalytic Applications

TEKETEL GIRMA GINDOSE*, and FANYANA M. MTUNZI

Department of Natural Sciences, Vaal University of Technology, Private Bag X021, Vanderbijlpark, 1911, South Africa

Corresponding author: E-mail: girmatek2007@gmail.com

Received: 6 July 2026 *Accepted*: 14 October 2026 *Published online*: 13 November 2026 AJC-22535

This study reports the fabrication of single-component ZnO, *g*-C_3N_4 and AgI photocatalysts as well as a ZnO-*g*-C_3N_4-AgI ternary heterojunction, for antimicrobial and photocatalytic activities. The synthesized nanomaterials were characterized using XRD, BET, FESEM-EDS, DRS and PL to analyze crystallite size, particle size distribution, surface area, surface morphology, band gap and electron-hole separation efficiency. The ZnO-*g*-C_3N_4-AgI composite exhibited the lowest band gap (2.39 eV), while ZnO showed the highest band gap energy (3.25 eV). This indicates that the formation of the ZnO-*g*-C_3N_4-AgI heterojunction effectively narrows the band gap, thereby enhancing light absorption and facilitating charge-carrier dynamics. The photocatalytic and antimicrobial performances of the prepared materials were also evaluated. The ZnO-*g*-C_3N_4-AgI demonstrated the highest methyl orange (MO) degradation efficiency (95%) and antimicrobial activity (24.25 ± 0.45 and 25.32 ± 0.52), which suggest a significant improvement in dye degradation efficiency compared to the individual components Antimicrobial assays revealed strong bacterial growth inhibition by the ternary ZnO-*g*-C_3N_4-AgI composite. Its proposed mechanism involves synergistic interactions among the three components that promote charge separation and reactive species generation. These features make the composite a potential candidate for environmental photocatalytic and antimicrobial applications.

Keywords: ZnO-*g*-C_3N_4-AgI, Antimicrobial, Photocatalysts, Heterojunction, Pollutants.

INTRODUCTION

Water is indispensable for human health, agricultural production and ecosystem stability [1]. Its quality is increasingly threatened by the discharge of organic pollutants from textile, pharmaceutical and food-processing industries [2-5]. The microbial contamination presents a parallel concern, as pathogenic microorganisms in polluted water can spread waterborne diseases and threaten public health [6-10]. The simultaneous presence of chemical contaminants and harmful microorganisms creates a need for wastewater treatment methods capable of addressing both problems. Conventional methods such as physical filtration and chemical disinfection, may not achieve complete contaminant removal under all operating conditions. Photocatalysis has attracted considerable attention for water purification due to its ability to degrade organic pollutants under light irradiation [11-19].

Semiconductor-based nanomaterials have been extensively studied for wastewater treatment due to their electronic, optical and surface properties [20-24]. Their photocatalytic performance depends on light absorption, band-gap energy, accessible surface area, chemical stability and charge-carrier dynamics. Beyond environmental remediation, these materials have applications in hydrogen generation through water splitting [25], energy storage [26] and energy conversion [27]. Despite their potential, the recovery of dispersed photocatalyst particles from treated water remains a practical limitation. Zinc oxide (ZnO) is a widely investigated semiconductor for organic pollutant degradation and microbial inactivation [28-31]. Its application is restricted by rapid electron–hole recombination and limited visible-light absorption. Doping and heterostructure formation have been explored to overcome these limitations [15,32-38]. Coupling ZnO with semiconductors such as ZnS [39,40], WO_3 [41], AgI [42], MnO_2 [43], CuO [44,45], Ag_3PO_4 [46], Fe_3O_4 [47,48] and Cu_2O [49] can modify interfacial charge transfer and improve photocatalytic performance. The extent of improvement depends on the band alignment, interfacial contact and composition of the resulting material.

Carbon-based heterostructures provide another approach to controlling charge-carrier behaviour [50]. Differences in

This is an open access journal, and articles are distributed under the terms of the Attribution 4.0 International (CC BY 4.0) License. This license lets others distribute, remix, tweak, and build upon your work, even commercially, as long as they credit the author for the original creation. You must give appropriate credit, provide a link to the license, and indicate if changes were made.

the electronic energy levels of the constituent semiconductors can promote directional charge transfer across their interfaces. In suitable systems, interfacial interactions and internal electric fields can facilitate electron–hole separation and reduce recombination losses [23]. Graphitic carbon nitride (*g*-C_3N_4) has attracted interest due to its relatively low cost, ease of synthesis, chemical stability and visible-light response [51]. Its photocatalytic potential has been investigated for bacterial inactivation [23] and dye degradation [24]. Rapid electron–hole recombination remains a limitation, reducing the availability of charge carriers for surface reactions. To address this problem, *g*-C_3N_4 has been combined with materials such as MnO_2 [25], ZnO [26], CuO [27], reduced graphene oxide (rGO) [28], CdS [29] and SnS_2 [52]. These combinations offer opportunities to modify charge transport and improve photocatalytic efficiency.

Silver iodide (AgI) has attracted interest in environmental applications due to its optical properties, antimicrobial activities and use in organic dye degradation [42,53-56]. Its incorporation into *g*-C_3N_4-based systems may modify interfacial charge transfer and improve charge-carrier separation [26]. Combining ZnO, *g*-C_3N_4 and AgI within a ternary heterostructure offers a means of integrating the properties of three semiconductors in a single photocatalytic system. The performance of such a composite depends on the interaction between its constituent phases, the quality of the interfaces and the efficiency of electron–hole separation. Particle aggregation can further limit performance by reducing accessible surface area and restricting contact between the photocatalyst and pollutants.

Polyvinyl alcohol (PVA) may help address material handling and dispersion challenges through its binding properties, water solubility, chemical stability and film-forming ability [57,58]. Its incorporation as a stabilizing agent or matrix may improve particle distribution and facilitate composite preparation. The actual effect of PVA depends on its concentration and mode of incorporation. Excessive polymer coverage may block active sites or restrict light access, making its role in photocatalytic performance an important factor to assess. In this study, a PVA-assisted ZnO-*g*-C_3N_4-AgI composite is investigated for the degradation of organic pollutants and the inactivation of harmful microorganisms in water. The material combines the complementary properties of ZnO, *g*-C_3N_4 and AgI, while PVA serves as a stabilizing or matrix component. The main contribution of this work lies in evaluating the ternary heterostructure for both photocatalytic and antimicrobial applications. Its performance must be assessed against the individual components and relevant binary composites to establish whether the combined system provides a measurable advantage. Structural and optical characterization, together with appropriate photocatalytic and antimicrobial tests, can clarify the role of the constituent materials and the contribution of the heterostructure to charge-carrier behaviour. The findings may establish the suitability of this PVA-assisted composite for further development in water-treatment applications.

EXPERIMENTAL

The chemicals and reagents *viz*. zinc acetate dihydrate ($Zn(CH_3COO)_2{\cdot}2H_2O$, purity ≥ 99.98%), ethanol (purity ≥ 96.5%), polyvinyl alcohol (purity ≥ 99%), sodium hydroxide, melamine ($C_3H_6N_6$, purity ≥ 98.56%), silver nitrate (purity ≥ 99.8%), potassium iodide (purity ≥ 99.5%), polyvinylpyrrolidone (PVP, $(C_6H_9NO)_n$, purity ≥ 99%) and hydrochloric acid (purity ≥ 37%) were used as starting materials. All chemicals were purchased from Sigma-Aldrich and used as received unless otherwise specified. Distilled water was used for washing throughout the experimental procedures.

Synthesis: Pure ZnO, *g*-C_3N_4 and AgI nanomaterials were synthesized using reported procedures [14,59]. The PVA-assisted ZnO-*g*-C_3N_4-AgI composite was fabricated by the sol-gel method. First, graphitic carbon nitride (*g*-C_3N_4) was prepared by heating melamine in a crucible at 550 ºC for 2 h. After cooling to room temperature, the resulting solid was ground into a fine powder. Separately, $Zn(CH_3COO)_2{\cdot}2H_2O$) was dissolved in a mixture of ethanol and distilled water. An ammonium solution was added to promote $Zn(OH)_2$ formation and the mixture was continuously stirred until a gel developed. The prepared *g*-C_3N_4 powder was incorporated into the $Zn(OH)_2$ gel under continuous mixing to achieve uniform dispersion. Silver nitrate and potassium iodide solutions were subsequently introduced to form AgI within the composite. Polyvinylpyrrolidone (PVP) was added as a nucleation controlling agent. The resulting mixture was transferred into a beaker containing a preheated PVA solution maintained at 100 ºC and magnetically stirred for 1 h. The mixture was then left to undergo gelation for 48 h. The resulting gel was filtered and washed with ethanol and distilled water to remove residual impurities before oven-drying. Finally, the dried material was annealed at 360 ºC to improve its crystallinity.

Characterization: The synthesized materials were characterized by X-ray diffraction (model no. 7000, Shimadzu, Japan) to identify their crystalline phases. Dynamic light scattering (DLS) was used to determine particle-size distribution in colloidal suspension. Diffuse reflectance spectroscopy (V-770, JASCO) was employed to examine optical absorption and estimate band-gap energy. Photoluminescence spectroscopy (FL 6500, Perkin-Elmer, USA) was used to assess charge carrier behaviour. Specific surface area and porosity were evaluated by Brunauer-Emmett-Teller (BET) analysis, while surface morphology was examined using field-emission scanning electron microscopy (JSM-6390LV, JEOL, Japan).

Photocatalytic analysis: The photocatalytic performance of the prepared materials was evaluated by degrading methylene orange (MO) under visible-light irradiation. In a typical experiment, an aqueous solution containing 15 mg/L of MO and 90 mg/L of each synthesized material was prepared in a beaker by dissolving them in 100 mL of distilled water. The suspension was kept in the dark for 30 min to achieve adsorption-desorption equilibrium. The mixture was then placed in the photoreactor and irradiated under magnetic stirring at room temperature. Subsequently, the samples were collected and separated from the photocatalyst by centrifugation. The remaining concentration of MO dye was analyzed using UV-Vis spectrophotometry. Operational parameters such as pH levels, initial dye concentration and catalyst load in the range of 2 to 12, 10 mg/L to 40 mg/L and 50 mg/L to 130 mg/L, respectively, were also measured. Furthermore, the stability and reusability of the photocatalyst were evaluated using the same

experimental protocol as the photocatalytic test. The photocatalyst's reusability was evaluated by repeatedly washing and drying it. Moreover, the photocatalytic process was conducted four times to assess the stability of the catalyst. The kinetic studies were also conducted to analyze the degradation rate. The experimental results were obtained using eqns. 1 and 2:

$$\text{Degradation (\%)} = \frac{C_o - C}{C_o} \times 100 \quad (1)$$

$$\ln \frac{C_o}{C} = K_{ap} t \quad (2)$$

where C_o and C_t represent the initial and time-dependent dye concentrations, respectively, while $k_{ap}t$ is the rate constant.

Antimicrobial test: In this study, the antimicrobial activity of ZnO, *g*-C_3N_4, AgI, ZnO-*g*-C_3N_4-AgI nanomaterials and ciprofloxacin was evaluated using the disc diffusion method. Mueller-Hinton agar (5 g) was dissolved in 100 mL of deionized water to prepare the nutrient agar medium, which was then autoclaved for 15 min at 121 ºC. Eight sterile plates were filled with autoclaved medium and allowed to cool to room temperature before solidifying. The antibacterial activity of ZnO, *g*-C_3N_4, AgI, ZnO-*g*-C_3N_4-AgI nanomaterials was evaluated against *Escherichia coli* and *Staphylococcus aureus* using the agar disc diffusion method. Sterile discs were soaked in nanomaterial suspensions prepared in DMSO at concentrations of 12.5, 25, 50 and 100 µg/mL and placed on inoculated agar plates. The plates were incubated at 37 ºC for 24 h. The antibacterial activity was assessed by measuring the inhibition zones in millimetres using calipers. All tests were performed in triplicate and the mean inhibition-zone diameters were compared to evaluate the antibacterial efficacy of the individual materials and the ternary composite [60].

RESULTS AND DISCUSSION

X-ray diffraction and dynamic light scattering (DLS) analysis: In this study, the XRD patterns of ZnO, *g*-C_3N_4, AgI and their composite ZnO-*g*-C_3N_4-AgI are shown in Fig. 1. The peaks at 31.67, 34.43, 36.32, 47.54, 56.66, 62.56, 66.21, 68.12 and 69.21º, corresponding to the Miller indices (*hkl*) (100), (002), (101), (102), (110), (103), (200), (112) and (201), respectively. These peaks correspond to the hexagonal wurtzite structure of ZnO (card no.: 00-062-0414) in the *P*63*mc* (186) space group. The XRD patterns of AgI exhibit distinct peaks that correspond to its cubic crystalline structure, with prominent peaks at 22.54º, 23.62º, 25.50º, 32.76º, 39.29º, 42.69º and 46.38º (2θ) (JCPDS No. 00 009-0399) [61], confirm the formation of the cubic phase of AgI in the ternary heterojunction system. For *g*-C_3N_4, a layered structure is evident, with prominent peak around 27.5º corresponding to the (002) planes, respectively [62]. The XRD pattern of the ZnO-*g*-C_3N_4-AgI composite revealed diffraction peaks corresponding to all three components, with ZnO appearing as a major crystalline phase. Variations in peak positions and intensities may arise from interfacial interactions among the constituents. The peak sharpness and intensity provide information on crystallinity, while peak broadening may be associated with crystallite size and lattice strain.

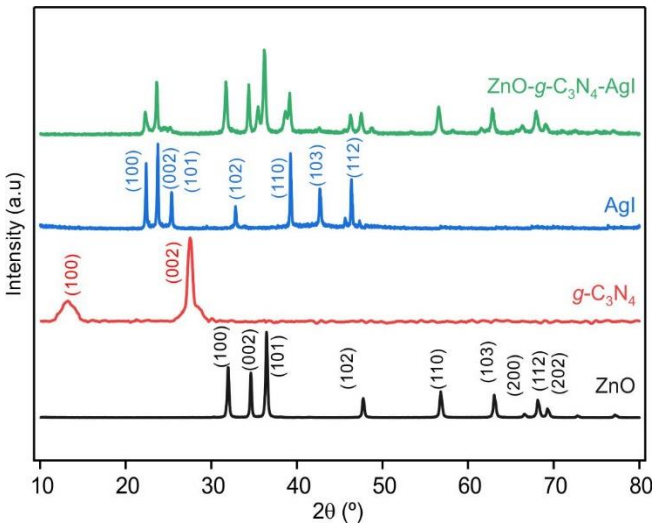


Fig. 1. XRD patterns of ZnO, *g*-C_3N_4, AgI and ZnO-*g*-C_3N_4-AgI nanocomposite

DLS analysis of ZnO, *g*-C_3N_4, AgI and ZnO-*g*-C_3N_4-AgI nanomaterials provides valuable insights into their particle-size distributions. The particle sizes for ZnO, *g*-C_3N_4, AgI and ZnO-*g*-C_3N_4-AgI photocatalysts were found to range from 10-29, 10–39, 24-97 and 20-110 nm, respectively (Fig. 2a-d). ZnO typically exhibits a specific particle-size range (Fig. 2a), which may vary with the synthesis method. In contrast, *g*-C_3N_4 usually shows a broader size distribution than ZnO (Fig. 2b) due to its layered structure, while AgI tends to have larger particle sizes (Fig. 2c) compared to both ZnO and *g*-C_3N_4. The smaller surface area of *g*-C_3N_4 helps reduce particle aggregation compared with the other pure samples prepared. The DLS results for the composite may reveal a shift in the size distribution compared to the individual components, indicating successful integration (Fig. 2d). Intensity variations were observed across all samples due to Brownian motion of the particles. These variations were analyzed to estimate the hydrodynamic diameter of the particles dispersed in the solution. The average hydrodynamic sizes of ZnO, *g*-C_3N_4, AgI and ZnO-*g*-C_3N_4-AgI were estimated to be 21, 19, 50 and 54 nm, respectively. The larger size of the ternary composite may arise from the combined presence of the three components and their interfacial interactions. The particle association through electrostatic attraction, surface adsorption or chemical bonding may contribute to this increase.

Surface morphology: In this study, nanomaterials such as ZnO, *g*-C_3N_3, AgI and their composite ZnO-*g*-C_3N_4-AgI were analyzed using FESEM (Fig. 3a-d). The FESEM images of ZnO, *g*-C_3N_3 and AgI samples typically reveal the flower-like spherical nanoparticles (Fig. 3a-c), although most samples exhibit a high degree of agglomeration. Specifically, the FESEM image of *g*-C_3N_4 shows a layered structure, whereas the FESEM image of the ZnO-*g*-C_3N_4-AgI composite analyzed reveals a remarkably uniform distribution of spherical nanoparticles with substantially reduced agglomeration (Fig. 3d). This improved dispersion in ZnO-*g*-C_3N_3-AgI is attributed to the strong stabilization capabilities of PVA, which effectively mitigates particle aggregation. The EDS spectrum and elemental mapping of the ZnO-*g*-C_3N_4-AgI composite was

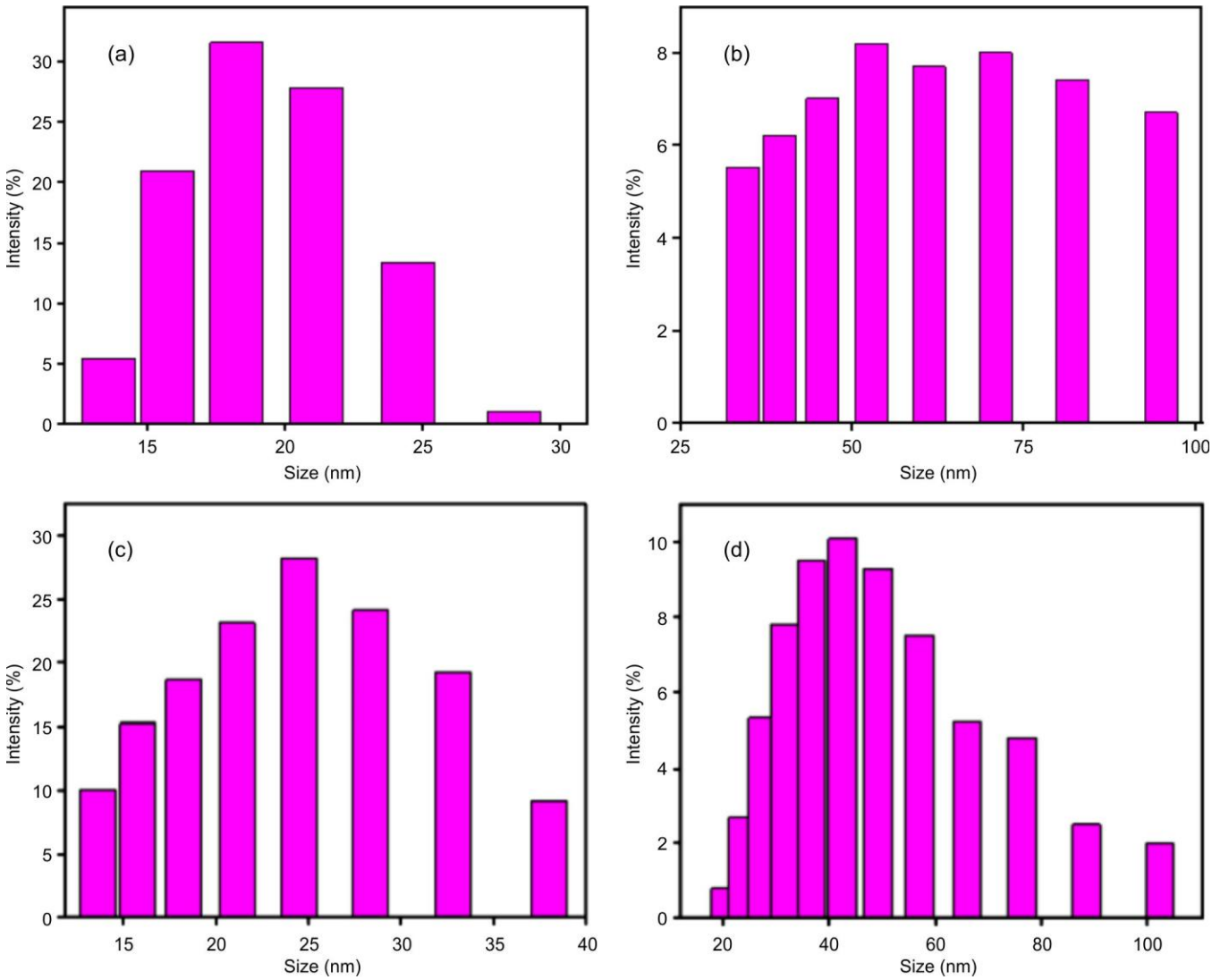


Fig. 2. DLS analysis of (a) ZnO, (b), *g*-C_3N_3, (c) AgI and (d) the ZnO-*g*-C_3N_4-AgI nanocomposite

also analyzed. Elemental analysis was performed using EDS to confirm the purity and compositional integrity of the synthesized materials. The EDS spectrum of the ZnO-*g*-C_3N_4-AgI nanocomposite (Fig. 3e) contains characteristic signals for Zn, C, Ag, I, N and O. The corresponding elemental composition is presented in the inset table of Fig. 3f. These results support the presence of the constituent elements identified in the composite. Elemental mapping images (Fig. 3f-k) further reveal their spatial distribution across the analyzed surface.

Brunauer-Emmett-Teller (BET) and diffuse reflectance spectroscopy (DRS) analysis: The surface properties, pore sizes and pore volume of individual ZnO, *g*-C_3N_4, AgI and the ZnO-*g*-C_3N_4-AgI composite were investigated using the N_2 adsorption/desorption technique. Fig. 4 illustrates that the N_2 adsorption-desorption isotherms of the four materials ZnO, *g*-C_3N_4, AgI and the composite ZnO-*g*-C_3N_4-AgI exhibit distinct Type IV isotherm features. This signifies the presence of mesoporous structures in all prepared samples. The BET specific surface areas of ZnO, *g*-C_3N_4, AgI and their composite ZnO-*g*-C_3N_4-AgI are 6.234 $m^2\ g^{-1}$, 8.365 $m^2\ g^{-1}$, 10.065 $m^2\ g^{-1}$ and 82.725 $m^2\ g^{-1}$, respectively. These findings show that the surface area of ZnO-*g*-C_3N_4-AgI is 13.3, 9.9 and 8.2 times higher than that of ZnO, *g*-C_3N_4 and AgI materials. Remarkably, the surface area of the ZnO-*g*-C_3N_4-AgI composite is improved. This may be ascribed to the formation of many pores on its surface. An increased specific surface area provides more active sites for photocatalytic reactions, thereby improving the efficacy of the photocatalytic process.

Optical analysis: Fig. 5a shows the absorption spectra of single ZnO, *g*-C_3N_4, AgI and ZnO-*g*-C_3N_4-AgI composite. Clearly, the absorption edge of single ZnO is observed in the ultraviolet region, whereas *g*-C_3N_4 and AgI exhibit the absorption edges found in the visible region. The absorption edge of ZnO shifts towards longer wavelengths after incorporation of *g*-C_3N_4 and AgI. This red shift extends the optical response into the visible region and may improve light absorption by the composite. The optical band gap (E_g) was estimated using the Tauc plot by extrapolating the linear region of the $(\alpha h\nu)^2$ *versus* hν plot (Fig. 5b), where hν denotes the photon energy and α represents the absorption coefficient. The DRS optical band gap energies, with ZnO showing a wide band gap (3.25

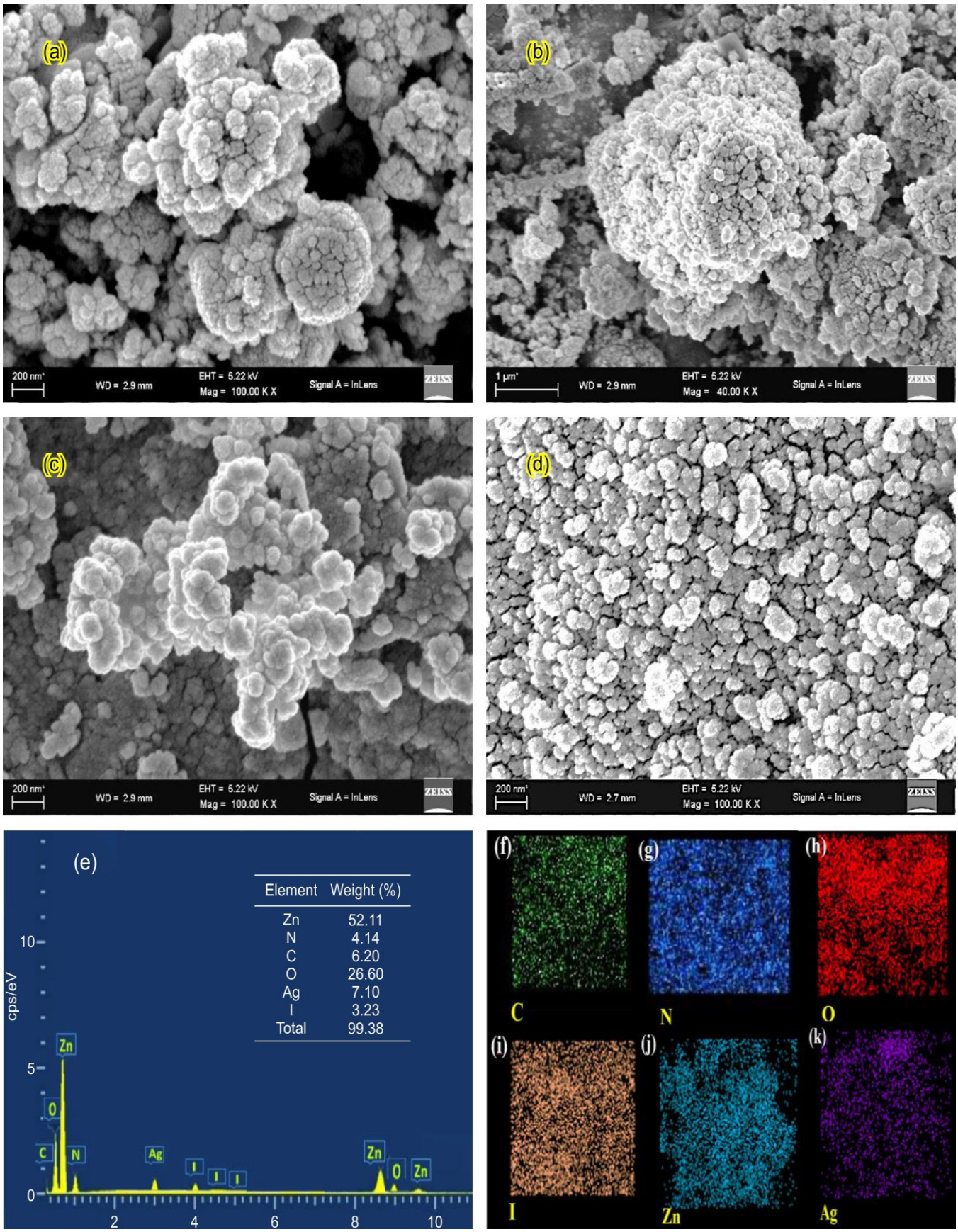


Fig. 3. FESEM images of (a) ZnO, (b) *g*-C_3N_4, (c) AgI, and (d) ZnO-*g*-C_3N_4-AgI composite; (e) EDS spectrum of ZnO-*g*-C_3N_4-AgI composite and its elemental mapping (f) carbon, (g) nitrogen, (h) oxygen, (i) iodine, (j) zinc and (k) silver in ZnO-*g*-C_3N_4-AgI nanocomposite

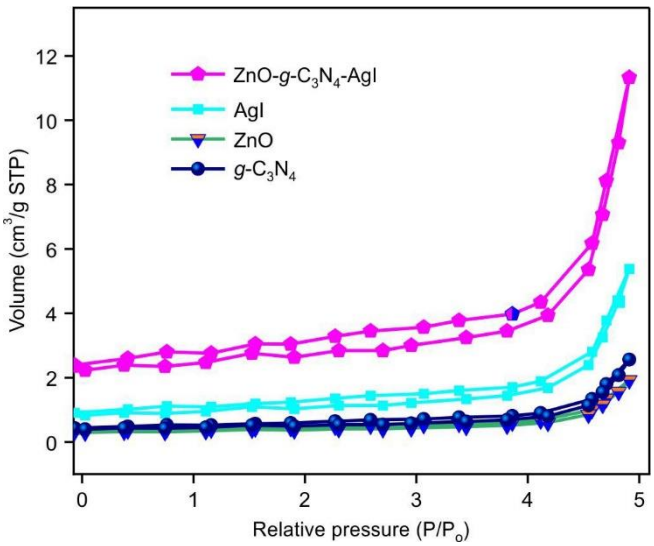


Fig. 4. Nitrogen adsorption–desorption plots of ZnO, *g*-C_3N_4, AgI, and ZnO-*g*-C_3N_4-AgI nanocomposite

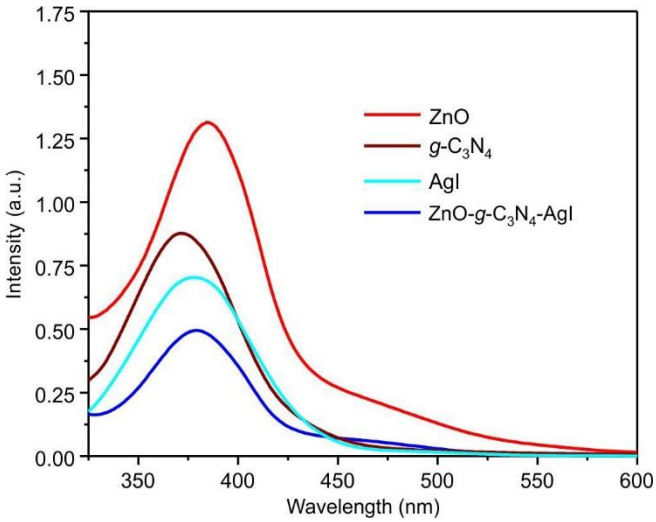


Fig. 6. PL spectra of the ZnO, *g*-C_3N_4, AgI, and ZnO-*g*-C_3N_4-AgI nanocomposite

eV) suitable for UV absorption *g*-C_3N_4 displaying a narrower band gap (2.74 eV) for visible light absorption and AgI around 2.68 eV. The optical band gap decreased from 3.25 eV for ZnO to 2.39 eV for the ZnO-*g*-C_3N_4-AgI composite. This reduction may extend light absorption into the visible region and improve the generation of photogenerated charge carriers, potentially enhancing photocatalytic and antibacterial performance.

Photoluminescence (PL) analysis: The PL spectra were recorded at an excitation wavelength of 350 nm to investigate the recombination behaviour of photogenerated electron–hole pairs in the synthesized materials (Fig. 6). All samples exhibited emission near 350 nm. Pure ZnO, *g*-C_3N_4 and AgI showed higher emission intensities than the ZnO-*g*-C_3N_4-AgI composite. The lower PL intensity of the ternary composite suggests reduced radiative recombination of photogenerated charge carriers, which may favour charge separation and interfacial charge transfer. This behaviour could enhance the availability of charge carriers for photocatalytic reactions. The PL intensity alone, though, cannot confirm longer carrier lifetimes or establish complete suppression of electron–hole recombination.

Photocatalytic study: The photocatalytic potentials of ZnO, *g*-C_3N_4, AgI and ZnO-*g*-C_3N_4-AgI photocatalysts were evaluated using MO dye as a target probe molecule under visible-light irradiation. Following 120 min of exposure to UV-vis light, the maximum degradation efficiency of ZnO, *g*-C_3N_4, AgI and ZnO-*g*-C_3N_4-AgI were 47%, 58%, 63% and 95%, respectively (Fig. 7a-b). The performance of ZnO-*g*-C_3N_4-AgI is 2.02, 1.64 and 1.51 times higher than that of ZnO, *g*-C_3N_4 and AgI photocatalysts, respectively. The enhanced degradation efficiency of the ZnO-*g*-C_3N_4-AgI photocatalyst comes from several key factors: (i) The combination of these materials creates synergistic effects that improve charge separation and reduce the recombination rates of electron-hole pairs; (ii) in addition, the ternary composite has a wider absorption range, which boosts its photocatalytic activity under visible light conditions; (iii) the increased surface area of the composite structure provides more active sites for the

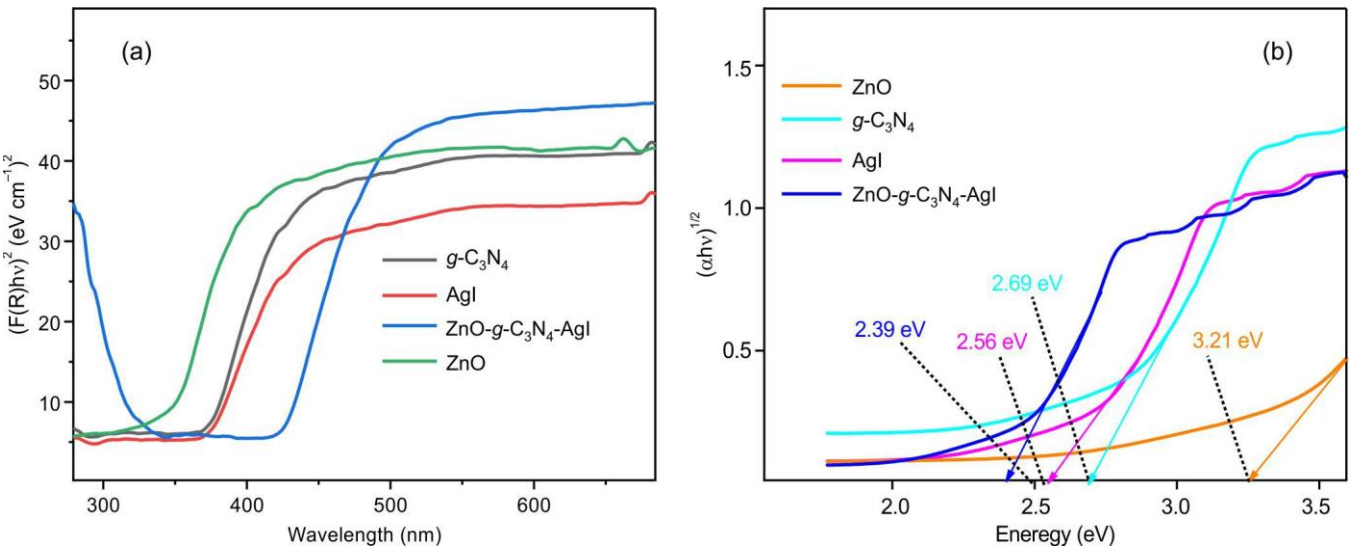


Fig. 5. UV-Vis DRS spectra (a) and Tauc plots (b) of ZnO, *g*-C_3N_3, AgI and ZnO-*g*-C_3N_4-AgI nanocomposite

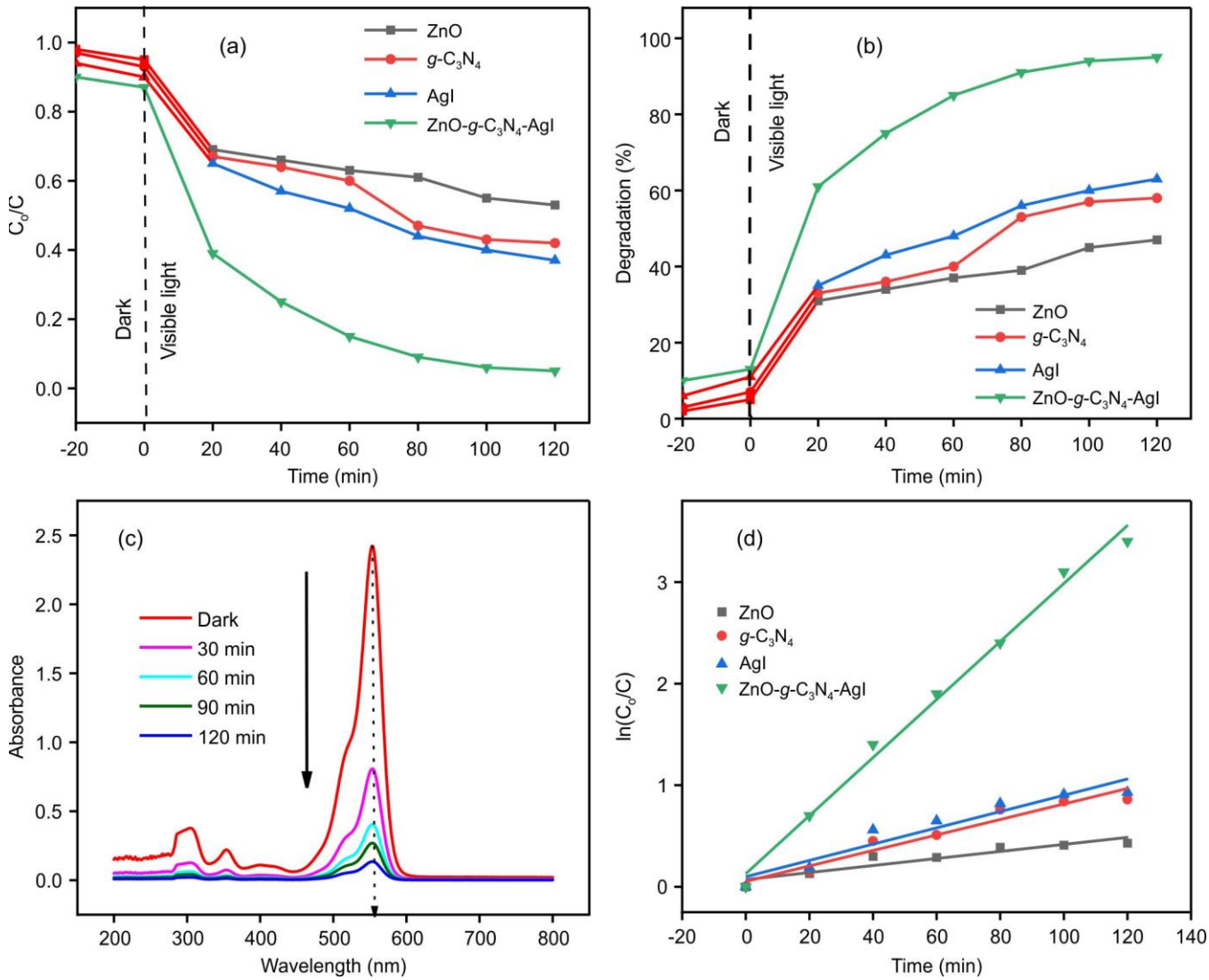


Fig. 7. (a) The removal efficiency of MO using ZnO, *g*-C_3N_4, AgI, and ZnO-*g*-C_3N_4-AgI photocatalyst, (b) highest % degradation, (c) UV spectra and (d) kinetic rate of MO as a function of time using 10 mg/L of MO and 90 mg/L of ZnO-*g*-C_3N_4-AgI composite under visible light irradiation

degradation reactions, further boosting efficiency; (iv) Moreover, the interaction between the components facilitates better mobility of charge carriers, which lead to the improved photocatalytic performance.

The UV-Vis spectra (Fig. 7c) exhibit a prominent absorption peak near 560 nm, with weaker absorption bands in the 250-350 nm region. The intensity of the main absorption peak decreases progressively from the dark condition to 120 min of irradiation. This decrease suggests a reduction in the concentration of the absorbing species during the reaction and may be associated with photocatalytic degradation of the pollutant. The gradual decrease in absorbance over time supports the photocatalytic activity of the composite.

Kinetic studies: The degradation data were fitted to a pseudo-first-order kinetic model (Fig. 7d). The rate constants for ZnO, *g*-C_3N_4, AgI and ZnO-*g*-C_3N_4-AgI were 0.0036, 0.0075, 0.0078 and 0.028 min^{-1}, respectively. The ternary composite exhibited a rate constant 7.8, 3.7 and 3.6 times higher than those of ZnO, *g*-C_3N_4 and AgI, respectively. The corresponding R^2 values were 0.87918, 0.94758, 0.91978 and 0.99194. The high R^2 value for the ternary composite indicates a strong fit to the pseudo-first-order model, while its higher rate constant reflects faster pollutant degradation under the tested conditions. These results support the enhanced photocatalytic performance of the ternary composite compared with the individual components.

Optimized parameters: The effects of solution pH, initial MO concentration and photocatalyst loading on photocatalytic efficiency were investigated to identify the optimal operating conditions. As shown in Fig. 8a, the degradation efficiency increased from 65% at pH 2 to 95% at pH 8, followed by a decrease at higher pH values. The optimum at pH 8 may be related to changes in catalyst surface charge and dye adsorption, which influence the availability of reactive species. The point of zero charge (pHpzc) was 7.47 (Fig. 8b). Above this pH, the catalyst surface is expected to become negatively charged, favouring the electrostatic attraction with cationic dye species. Since, MO is generally an anionic dye under

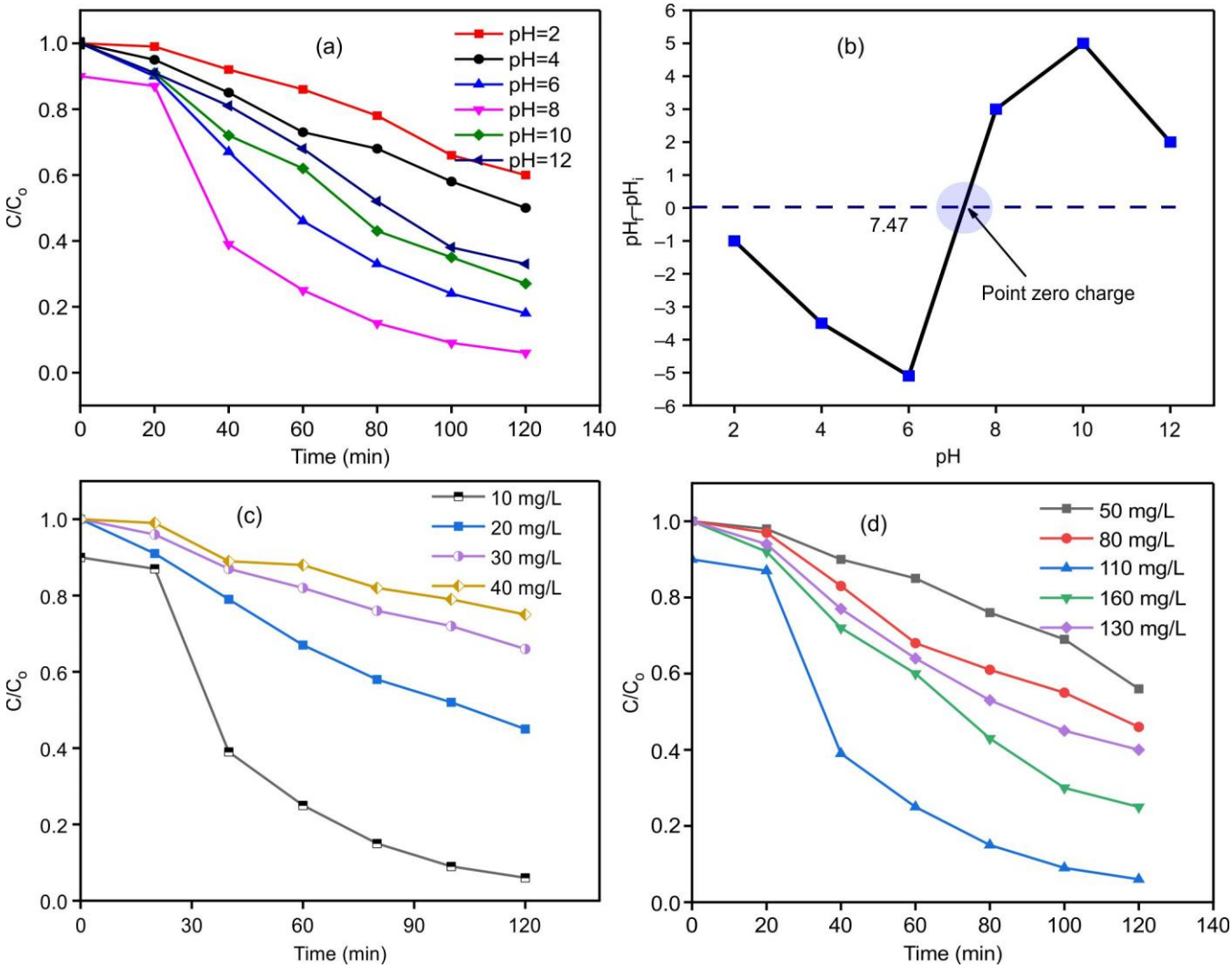


Fig. 8. (a) Effect of pH, (b) point zero charge, (c) effects of initial dye concentration of MO and (d) effect of catalyst loading

typical aqueous conditions, the proposed adsorption mechanism should be reconsidered in light of its charge state and the solution pH.

The initial MO concentration was varied from 10 to 40 mg/L. As shown in Fig. 8c, the degradation efficiency decreased with increasing dye concentration. A higher concentration of dye can limit light penetration and reduce the light reaching the catalyst surface, which restrict the generation of photogenerated charge carriers and reactive species. The effect of photocatalyst loading was examined under similar reaction conditions (Fig. 8d). Degradation efficiency increased as the catalyst dosage rose from 80 to 110 mg/L, which is likely due to the higher availability of active sites. At higher loading, the efficiency declined, which may be associated with particle agglomeration, light scattering and reduced light penetration through the suspension.

Stability and reusability test: The ZnO-*g*-C_3N_4-AgI composite was tested over four consecutive photocatalytic cycles. As shown in Fig. 9a, MO dye degradation efficiency decreased from 95% in the first cycle to 94%, 93% and 90.4% in the second, third and fourth cycles, respectively. The gradual decline indicates a modest loss of photocatalytic activity during repeated use. The composite retained 90.4% degradation efficiency after four cycles, which suggest the reasonable reusability under the tested conditions. Its stability was further examined by comparing the diffuse reflectance spectra (DRS; Fig. 9b) and X-ray diffraction patterns (Fig. 10) before and after recycling to assess changes in the optical properties and crystal structure.

Mechanisms: The radical-scavenging experiments were conducted to identify the reactive species responsible for MO photodegradation. EDTA, benzoquinone (BQ) and isopropyl alcohol (IPA) were used to scavenge photogenerated holes (h^+), superoxide radicals ($^\bullet O_2^-$) and hydroxyl radicals ($^\bullet OH$), respectively. The experiments were performed using a dye concentration of 10 mg/L and a photocatalyst loading of 90 mg/L in 60 mL of solution. As shown in Fig. 11, the degradation efficiency decreased from 95% in the absence of scavengers to 31.2%, 35% and 51% in the presence of IPA, BQ and EDTA, respectively. The pronounced decline in the presence of IPA and BQ points to the major contributions of $^\bullet OH$ and $^\bullet O_2^-$ to dye degradation, while the reduction caused by EDTA confirms the involvement of photogenerated holes. The conduction band (CB) and valence band (VB) potentials of the

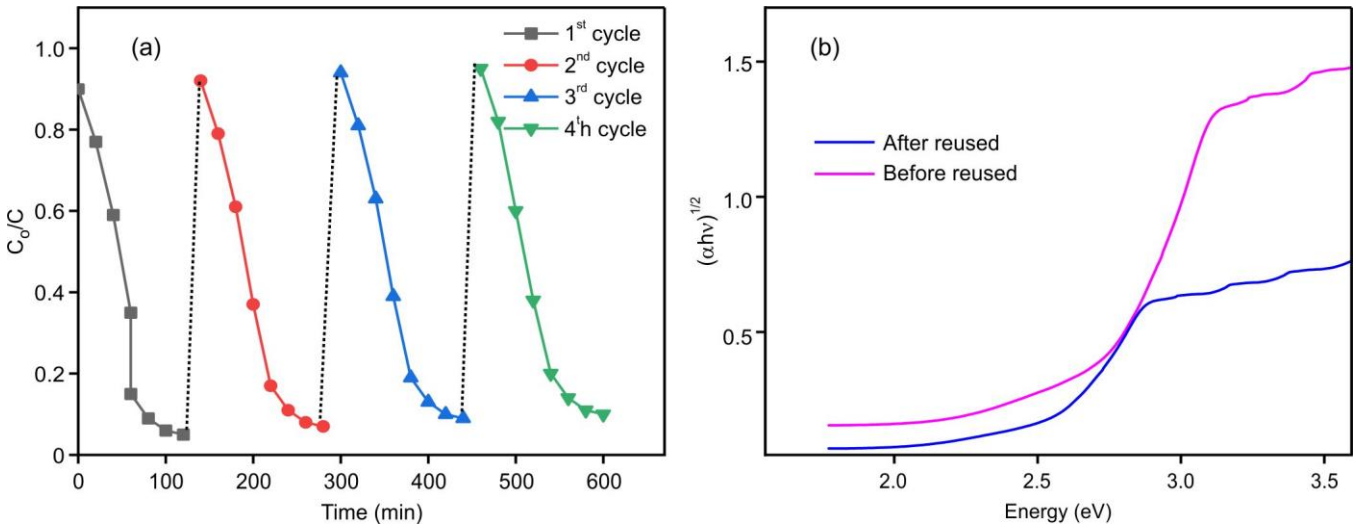


Fig. 9. Plots of recyclability and stability analysis of ZnO-*g*-C_3N_4-AgI

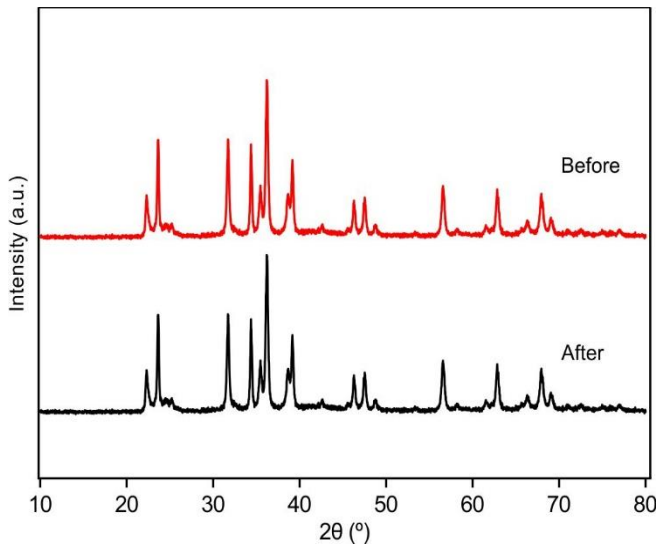


Fig. 10. XRD spectra of ZnO-*g*-C_3N_4-AgI nanomaterials before and after recycling

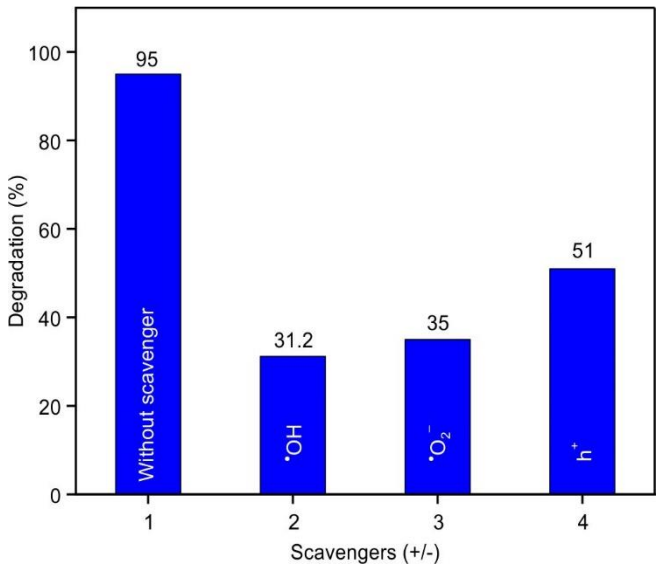


Fig. 11. Effect of different scavengers on MO photodegradation

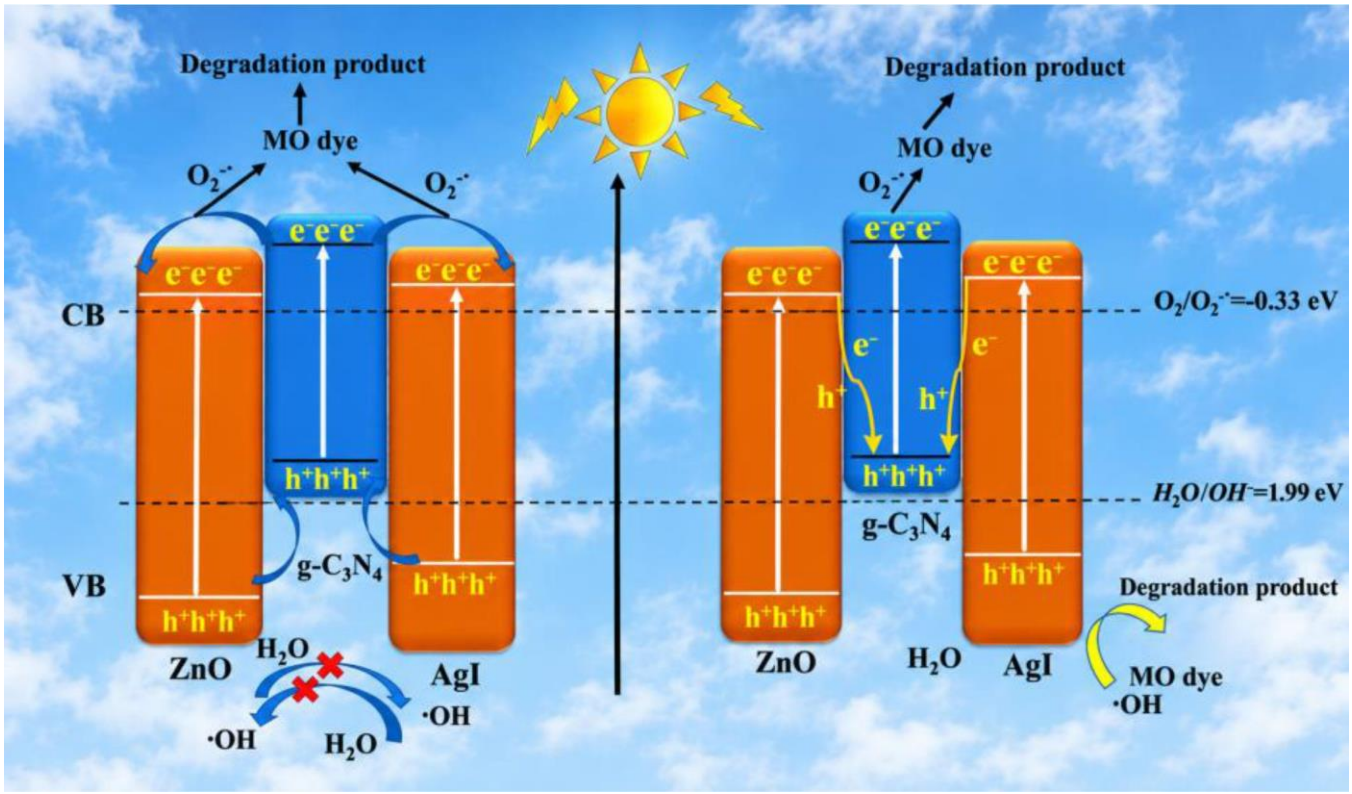
individual semiconductors were estimated using their band-gap energies obtained from the Tauc plots and the electronegativity-based equations:

$$E_{CB} = \chi - E_e - \frac{1}{2}E_g$$

$$E_{VB} = E_{CB} + E_g$$

Here, χ represents the absolute electronegativity of the semiconductor, E_e is the energy of free electrons on the hydrogen scale (4.5 eV) and E_g is the optical band-gap energy. The calculated CB and VB potentials were -0.34 and +2.92 V for ZnO, −0.37 and +2.33 V for AgI, and -1.14 and +1.60 V for *g*-C_3N_4, respectively. These values provide a basis for examining the possible charge-transfer pathways in the ternary composite. Under illumination, electrons in the VB of each semiconductor can be excited to its CB, leaving holes in the VB. In a conventional type-II heterojunction, electrons transfer from the CB of *g*-C_3N_4 to the CBs of ZnO and AgI, while holes migrate from the VBs of ZnO and AgI to the VB of *g*-C_3N_4. Although this pathway promotes charge separation, it reduces the redox potential of the surviving electrons and holes. The CB potentials of ZnO and AgI may limit their ability to generate reactive oxygen species, while the VB potential of *g*-C_3N_4 is insufficient for efficient hydroxyl radical generation from water or hydroxide ions. These limitations make a conventional type-II pathway less consistent with strong radical-mediated degradation.

A Z-scheme mechanism may better explain the retention of strong redox potentials in the ternary composite. In this pathway, electrons in the CBs of ZnO and AgI recombine with holes in the VB of *g*-C_3N_4, leaving highly reducing electrons in the CB of *g*-C_3N_4 and strongly oxidizing holes in the VB of ZnO. The remaining electrons may reduce dissolved oxygen to $^{\bullet}O_2^-$, while the holes in ZnO may promote $^{\bullet}$OH formation under suitable conditions. These reactive species can attack dye molecules and facilitate their degradation. The scavenging results are consistent with the involvement of both radicals (**Scheme-I**).

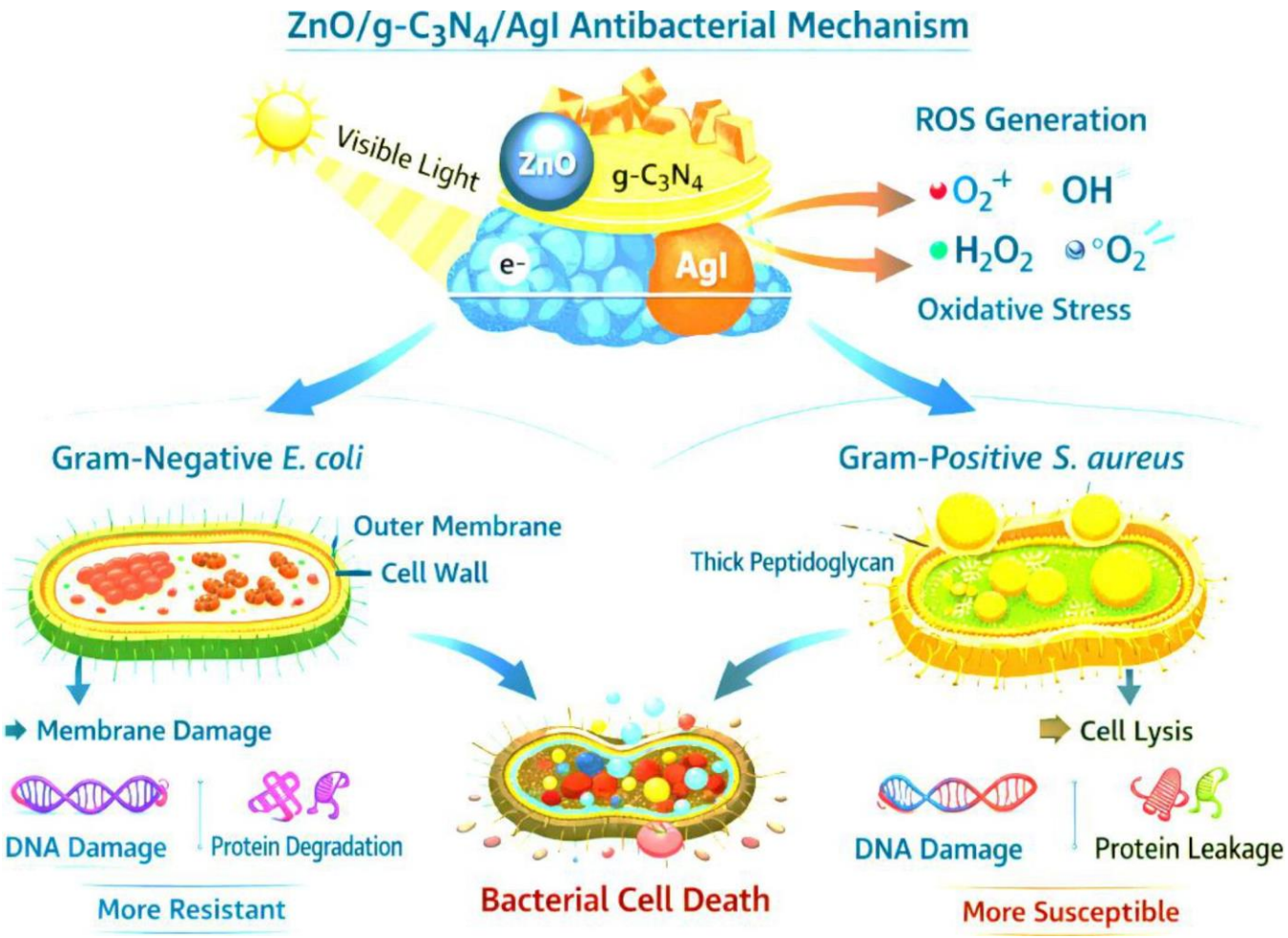


Scheme-I: Proposed heterojunction structure of the electron–hole and transfers in the photodegradation reaction over ZnO-*g*-C_3N_4-AgI nanocomposite

Antimicrobial test: The antibacterial potential of ZnO, *g*-C_3N_4, AgI, ZnO-*g*-C_3N_4-AgI and ciprofloxacin was evaluated against *E. coli* and *S. aureus*. All samples exhibited a clear dose-dependent inhibition, with inhibition zones (IZ) expanding proportionally from 12.5 to 100 µg/mL. At the highest concentration (100 µg/mL), the ZnO-*g*-C_3N_4-AgI nanocomposite showed superior antibacterial potential, producing IZ values of 24.25 ± 0.45 mm against *E. coli* and 25.32 ± 0.52 mm against *S. aureus*. According to these findings, the composite is almost as effective as ciprofloxacin, which at 100 µg/mL demonstrated 24.62 ± 0.37 and 25.75 ± 0.32 against *E. coli* and *S. aureus*, respectively. The enhanced antibacterial activity of the ZnO-*g*-C_3N_4-AgI composite, compared to its individual components, can be attributed to synergistic effects that enhance photocatalytic performance and the generation of reactive oxygen species (ROS) [63]. Furthermore, the results of the AgI, *g*-C_3N_4 and ZnO tests also demonstrate strong activity. However, as AgI has a lower bandgap and generates more ROS under visible light, it is more effective against both bacterial strains than *g*-C_3N_4 and ZnO nanoparticles. Compared to ZnO nanoparticles, *g*-C_3N_4 nanoparticles displayed somewhat larger inhibitory zones. The observed IZ values against *E. coli* and *S. aureus* at 100 µg/mL are 15.32 ± 0.54 and 16.31 ± 0.37 for ZnO, 16.14 ± 0.48 and 17.11 ± 0.59 for *g*-C_3N_4 and 17.13 ± 0.65 and 18.14 ± 0.68 for AgI, as shown in Table-1. Gram-positive *S. aureus* was more susceptible to the treatments than Gram-negative *E. coli* across all tests. This difference may be related to their cell envelope structures. The outer membrane of Gram-negative bacteria acts as an additional barrier to antimicrobial agents, whereas Gram-positive bacteria lack this membrane and may be more vulnerable to treatment [64,65]. The results indicate stronger antibacterial activity of the ZnO-*g*-C_3N_4-AgI nanocomposite against *S. aureus* under the tested conditions. The proposed antibacterial mechanisms of the prepared materials against Gram-positive and Gram-negative bacteria are illustrated in **Scheme-II**.

TABLE-1
INHIBITION ZONE (mm) OF ZnO, *g*-C_3N_4, AgI, ZnO-*g*-C_3N_4-AgI AND CIPROFLOXACIN AGAINST *E. coli* AND *S. aureus*

Antibacterial agent	Conc. (µg/mL)	Gram-negative bacteria (*E. coli*)	Gram-positive bacteria (*S. aureus*)
ZnO	12.5	9.11 ± 0.38	10.06 ± 0.30
	25	10.88 ± 0.28	12.30 ± 0.55
	50	13.10 ± 0.42	14.10 ± 0.45
	100	15.32 ± 0.54	16.31 ± 0.37
g-C_3N_4	12.5	9.57 ± 0.58	10.43 ± 0.45
	25	11.22 ± 0.34	12.72 ± 0.57
	50	13.87 ± 0.62	14.51 ± 0.41
	100	16.14 ± 0.48	17.11 ± 0.59
AgI	12.5	10.41 ± 0.52	12.12 ± 0.46
	25	12.12 ± 0.43	13.56 ± 0.48
	50	15.21 ± 0.61	16.21 ± 0.28
	100	17.13 ± 0.65	18.14 ± 0.68
ZnO-*g*-C_3N_4-AgI	12.5	13.36 ± 0.41	15.08 ± 0.42
	25	16.32 ± 0.51	18.22 ± 0.47
	50	20.41 ± 0.62	21.12 ± 0.28
	100	24.25 ± 0.45	25.32 ± 0.52
Ciprofloxacin	100	24.62 ± 0.37	25.75 ± 0.32



Scheme-II: Proposed antimicrobial mechanisms

Conclusion

This study investigated the synthesis and characterization of ZnO, *g*-C_3N_4 and AgI, along with the development of a ZnO-*g*-C_3N_4-AgI ternary nanocomposite. The nanocomposite exhibited a reduced band gap of 2.39 eV, achieved 95% dye degradation and also showed stronger antibacterial activity than the individual components under the tested conditions. The enhanced performance may be associated with interactions among the three semiconductors and changes in charge-carrier behaviour. Radical-scavenging experiments identified $^{\bullet}OH$, $^{\bullet}O_2^-$ and photogenerated holes as contributors to dye degradation. The proposed charge-transfer mechanism offers a possible explanation for the observed photocatalytic activity.

CONFLICT OF INTEREST

The authors declare that there is no conflicts of interest regarding the publication of this article.

DECLARATION OF AI-ASSISTED TECHNOLOGIES

During the preparation of this manuscript, the authors used an AI-assisted tool(s) to improve the language and no data, results or scientific conclusions were generated by AI. All analyses, interpretations and conclusions are the authors' own. The authors reviewed and edited the content and take full responsibility for the published work.

REFERENCES

1. P. Kumar, V. Kumar and V. Dhiman, *Sustain. Chem. Clim. Action*, **7**, 100110 (2025); https://doi.org/10.1016/j.scca.2025.100110
2. Z. Niaz, R. Tariq and G.A. Chotana, *RSC Adv.*, **13**, 35537 (2023); https://doi.org/10.1039/D3RA06109D
3. A. Taravati, A.P. Marjani, S. Bibak and H.S. Aslaheh, *Sci. Rep.*, **15**, 36817 (2025); https://doi.org/10.1038/s41598-025-23196-4
4. S. Yadav, K.S. Tiwari, C. Gupta, M.K. Tiwari, A. Khan and S.P. Sonkar, *Results Chem.*, **5**, 100733 (2023); https://doi.org/10.1016/j.rechem.2022.100733
5. A.M. Hamza, H.A. Alshamsi, *Sci. Rep.*, **14**, 23596 (2024); https://doi.org/10.1038/s41598-024-73915-6
6. Y. Cong, Y. Li, X. Wang, X. Wei, L. Che and S. Lv, *Sep. Purif. Technol.*, **297**, 121531 (2022); https://doi.org/10.1016/j.seppur.2022.121531
7. S. Lakshmanaprabhu, D. Ganesan, K. Priyadharshini and S. Hemavathi, *Glob. NEST J.*, **26**, 05411 (2023); https://doi.org/10.30955/gnj.005411
8. A. Bosveli, T. Montagnon, D. Kalaitzakis and G. Vassilikogiannakis, *Org. Biomol. Chem.*, **19**, 3303 (2021); https://doi.org/10.1039/D1OB00301A

9. A.H. Kamel, H.S.M. Abd-Rabboh, A. Abd El-Fattah, G. Boudghene Stambouli and L. Adeida, *RSC Adv.*, **15**, 6875 (2025); https://doi.org/10.1039/D4RA08149H
10. F.S. Abdulwahid, A.H. Attallah, M.K. Abood and A.J. Haider, *Photochem. Photobiol. Sci.*, **24**, 1959 (2025); https://doi.org/10.1007/s43630-025-00808-6
11. T.P. Vijayakumar, M.D. Benoy, J. Duraimurugan, G. Suresh Kumar, M. Shkir, P. Maadeswaran, A. Senthil Kumar and K.A. Ramesh Kumar, *Diamond Relat. Mater.*, **121**, 108735 (2022); https://doi.org/10.1016/j.diamond.2021.108735
12. O. Fawzi Suleiman Khasawneh and P. Palaniandy, *Environ. Technol. Innov.*, **21**, 101230 (2021); https://doi.org/10.1016/j.eti.2020.101230
13. N. Qutub, P. Singh, S. Sabir, S. Sagadevan and W.-C. Oh, *Sci. Rep.*, **12**, 5759 (2022); https://doi.org/10.1038/s41598-022-09479-0
14. T.G. Gindose, B. Mothudi, K.H. Tolera, M. Feyissa, M.E. Kassa, H.G. Abebe, A.P. Agnès, F. Mukhtar and N.A. Lebachew, *ChemistrySelect*, **11**, e07415 (2026); https://doi.org/10.1002/slct.202507415
15. T.G. Gindose, E.A. Zereffa, T.B. Atisme, T. Sani and T.D. Hailegebreal, *Adv. Mater. Sci. Eng.*, **2025**, 9925834 (2025); https://doi.org/10.1155/amse/9925834
16. T.G. Gindose, T.B. Atisme, G. Gebreslassie, A.B. Gebresilassie and E.A. Zereffa, *Mater. Adv.*, **5**, 8017 (2024); https://doi.org/10.1039/D4MA00357H
17. T.G. Gindose, B.M. Mothudi, M.E. Kassa, E.A. Zereffa, A.M. Taddesse, K.N. Mekonnen, A.K. Ebrahim, F.M. Mtunzi, E.N. Nxumalo, T.G. Ashebr, T.B. Atisme, E.K. Suter, T. Dessalegn and M.R. Habib, *Adv. Mater. Sci. Eng.*, **2026**, 5469069 (2026); https://doi.org/10.1155/amse/5469069
18. W. Xie, G. Liu, Y. Liu, Y. Bai, Y. Liao, T. Li, C. Wang, S. Chang and J. Hu, *J. Porous Mater.*, **31**, 1655 (2024); https://doi.org/10.1007/s10934-024-01619-3
19. A. Wafi, L. Roza, G. E. Timuda, D. Aji, D. S. Khaerudini, N. Darsono, N. Yudasari, E. Szabó-Bárdos, O. Horváth and M. M. Khan, *Transition Met. Chem.*, **49**, 305 (2024); https://doi.org/10.1007/s11243-024-00584-9
20. C. Huang and J. Li, *ECS J. Solid State Sci. Technol.*, **12**, 076009 (2023); https://doi.org/10.1149/2162-8777/ace654
21. P. Nandi and D. Das, *J. Phys. Chem. Solids*, **160**, 110344 (2022); https://doi.org/10.1016/j.jpcs.2021.110344
22. T.G. Gindose, G. Gebreslassie, T.D. Hailegebreal, T.G. Ashebr, F. Mtunzi, T.B. Atisme and E.A. Zereffa, *RSC Adv.*, **14**, 38459 (2024); https://doi.org/10.1039/D4RA06476C
23. T.G. Gindose, T.B. Atisme, T.D. Hailegebreal and E.A. Zereffa, *ChemistrySelect*, **10**, e202403418 (2025); https://doi.org/10.1002/slct.202403418
24. D.G. Ayu, S. Gea, N. Andriayani, D.J. Telaumbanua, A.F.R. Piliang, M. Harahap, Z. Yen, R. Goei and A.I.Y. Tok, *ACS Omega*, **8**, 14965 (2023); https://doi.org/10.1021/acsomega.2c07546
25. F. Bhom and Y.M. Isa, *Glob. Chall.*, **8**, 2400134 (2024); https://doi.org/10.1002/gch2.202400134
26. A. Meftahi, M. Shabani-Nooshabadi and A. Reisi-Vanani, *Electrochim. Acta*, **430**, 141052 (2022); https://doi.org/10.1016/j.electacta.2022.141052
27. B. Wang, Z. Chen, J. Zhang, J. Cao, S. Wang, Q. Tian, M. Gao and Q. Xu, *Colloids Surf. A Physicochem. Eng. Asp.*, **457**, 318 (2014); https://doi.org/10.1016/j.colsurfa.2014.06.006
28. S.K. Nadikatla, V.B. Chintada, T.R. Gurugubelli and R. Koutavarapu, *Molecules*, **28**, 4277 (2023); https://doi.org/10.3390/molecules28114277
29. K.A. Adegoke, M. Iqbal, H. Louis and O.S. Bello, *Mater. Sci. Energy Technol.*, **2**, 329 (2019); https://doi.org/10.1016/j.mset.2019.02.008
30. F.M. Mtunzi, N.D. Shooto, B.J. Okoli, J. Kumar and T.G. Gindose, *J. Photochem. Photobiol.*, **31**, 100273 (2026); https://doi.org/10.1016/j.jpap.2025.100273
31. M.S. Saif, A. Zafar, M. Waqas, S.G. Hassan, A. ul Haq, T. Tariq, S. Batool, M. Dilshad, M. Hasan and X. Shu, *J. Mater. Res. Technol.*, **13**, 2375 (2021); https://doi.org/10.1016/j.jmrt.2021.05.107
32. A.T. Vu, V.H. Mac, T.H. Nguyen and T.H. Nguyen, *Nanotechnology*, **34**, 275602 (2023); https://doi.org/10.1088/1361-6528/acca24
33. A. Gaurav, R. Beura, J.S. Kumar and P. Thangadurai, *Mater. Chem. Phys.*, **230**, 162 (2019); https://doi.org/10.1016/j.matchemphys.2019.03.056
34. G. Chen, M. Yang, B. Tian, J. Yao, S. Chen, D. Li and G. Yuan, *Sci. Rep.*, **15**, 18246 (2025); https://doi.org/10.1038/s41598-025-02432-x
35. M. Ding, N. Yao, C. Wang, J. Huang, M. Shao, S. Zhang, P. Li, X. Deng and X. Xu, *Nanoscale Res. Lett.*, **11**, 205 (2016); https://doi.org/10.1186/s11671-016-1432-7
36. F. Pinzari, *Reactions*, **5**, 680 (2024); https://doi.org/10.3390/reactions5040035
37. Z. Luo, X. Guo, W. Chen, Q. Feng, C. Qi and P. Li, *Phys. Status Solidi A Appl. Mater. Sci.*, **222**, 1 (2025); https://doi.org/10.1002/pssa.202400957
38. A. Sarker, S.A. Fahim, R.A. Putul, H. Gazi, S.M. Masum and M.A.I. Molla, *Next Nanotechnol.*, **8**, 100146 (2025); https://doi.org/10.1016/j.nnano.2025.100146
39. X. Li, X. Li, B. Zhu, J. Wang, H. Lan and X. Chen, *RSC Adv.*, **7**, 30956 (2017); https://doi.org/10.1039/C7RA03243A
40. X. Jin, J. Chen, F. Chen, H. Duan, Z. Wang and J. Li, *Catalysts*, **12**, 981 (2022); https://doi.org/10.3390/catal12090981
41. S. Adhikari, D. Sarkar and G. Madras, *RSC Adv.*, **5**, 11895 (2015); https://doi.org/10.1039/C4RA13210F
42. C. Ding, K. Fu, Y. Pan, J. Liu, H. Deng and J. Shi, *Catalysts*, **10**, 1097 (2020); https://doi.org/10.3390/catal10091097
43. M.E. Kassa, E.A. Zereffa, T.G. Gindose and T.D. Zeleke, *Sci. Rep.*, **16**, 5078 (2026); https://doi.org/10.1038/s41598-025-34955-8
44. Z.S. Seddigi, U. Baig, J.A. Khan and M.A. Gondal, *Arab. J. Sci. Eng.*, **50**, 3925 (2025); https://doi.org/10.1007/s13369-024-09294-x
45. R. Saravanan, S. Karthikeyan, V.K. Gupta, G. Sekaran, V. Narayanan and A. Stephen, *Mater. Sci. Eng. C*, **33**, 91 (2013); https://doi.org/10.1016/j.msec.2012.08.011
46. C. Dong, K. Wu, M. Li, L. Liu and X. Wei, *Catal. Commun.*, **46**, 32 (2014); https://doi.org/10.1016/j.catcom.2013.11.018
47. X. Ji, Y. Han, Y. Wu, B. Liang, J. Zheng, S. Ma, C. Li, H. Xu and S. Guo, *Environ. Sci. Pollut. Res. Int.*, **30**, 87016 (2023); https://doi.org/10.1007/s11356-023-28534-5
48. M.E. Kassa, T.G. Gindose, E. Zereffa, G. Amenu, M. Adem and T. Desalegn, *R. Soc. Open Sci.*, **13**, 251309 (2026); https://doi.org/10.1098/rsos.251309
49. Y. Wang, J. Gao, X. Wang, L. Jin, L. Fang, M. Zhang, G. He and Z. Sun, *J. Sol-Gel Sci. Technol.*, **88**, 172 (2018); https://doi.org/10.1007/s10971-018-4786-8
50. S. Thaweesak, S. Wang, M. Lyu, M. Xiao, P. Peerakiatkhajohn and L. Wang, *Dalton Trans.*, **46**, 10714 (2017); https://doi.org/10.1039/C7DT00933J
51. D. Bhanderi, P. Lakhani and C.K. Modi, *RSC Sustain.*, **2**, 265 (2024); https://doi.org/10.1039/D3SU00382E
52. F. Deng, L. Zhao, X. Pei, X. Luo and S. Luo, *Mater. Chem. Phys.*, **189** 169 (2017); https://doi.org/10.1016/j.matchemphys.2016.12.028
53. M.Z.A. Warshagha, M. Muneer, I.I. Althagafi and S.A. Ahmed, *RSC Adv.*, **13**, 5013 (2023); https://doi.org/10.1039/D2RA07626H
54. J. Jiang, L. Yu, J. Peng, W. Gong and W. Sun, *Carbon Lett.*, **35**, 417 (2025); https://doi.org/10.1007/s42823-024-00853-8
55. S. Husein, Slamet and E.L. Dewi, *Waste Dispos. Sustain. Energy*, **6**, 603 (2024); https://doi.org/10.1007/s42768-024-00198-y
56. A.A.P. Khan, A. Sonu, A. Sudhaik, P. Raizada, A. Khan, M.A. Rub, N. Azum, M.M. Alotaibi, P. Singh and A.M. Asiri, *Catal. Commun.*, **179**, 106685 (2023); https://doi.org/10.1016/j.catcom.2023.106685

57. B. Abebe, H.C. Ananda Murthy, E. Zerefa and E. Abdisa, *Mater. Res. Express*, **7**, 065002 (2020); https://doi.org/10.088/2053-1591/ab94fc
58. T.G. Gindose, G. Gebreslassie, T. Derbe, T.G. Ashebr, Y.T. Daba, F.M. Mtunzi, T. Xaba, H.L. Rutto, E.A. Zereffa and T.B. Atisme, *Results Chem.*, **16**, 102327 (2025); https://doi.org/10.1016/j.rechem.2025.102327
59. G. Gindose, T.G. Admasu, E.A. Zereffa, T.G. Ashebr, F.E. Ayamlo, F. K. Sabir, F.M. Mtunzi, E.N. Nxumalo, B. Alemu, T.A. Orshiso and T.B. Atisme, *J. Sci. Adv. Mater. Devices*, **10**, 101026 (2025); https://doi.org/10.1016/j.jsamd.2025.101026
60. G. Tadesse, H.C. Ananda Murthy, C.R. Ravikumar, T. Naveen Kumar, L. Teshome and T. Desalegn, *Bioinorg. Chem. Appl.*, **2023**, 5019838 (2023); https://doi.org/10.1155/2023/5019838
61. J. Zhang and Z. Ma, *Mater. Lett.*, **216**, 216 (2018); https://doi.org/10.1016/j.matlet.2018.01.035
62. F. Zhang, L. Huang, P. Ding, C. Wang, Q. Wang, H. Wang, Y. Li, H. Xu and H. Li, *J. Alloys Compd.*, **795**, 426 (2019); https://doi.org/10.1016/j.jallcom.2019.04.297
63. D. Shao and Q. Wei, *Materials*, **11**, 1412 (2018); https://doi.org/10.3390/ma11081412
64. T.A. Orshiso, D.B. Adamu, T.G. Gindose, T. Kiros, A. Zelalam and E.A. Zereffa, *J. Photochem. Photobiol.*, **36**, 100312 (2026); https://doi.org/10.1016/j.jpap.2026.100312
65. Z. Breijyeh, B. Jubeh and R. Karaman, *Molecules*, **25**, 2888 (2020); https://doi.org/10.3390/molecules25122888